Lab on a Chip

PAPER

View Article Online
View Journal | View Issue

Cite this: *Lab Chip*, 2021, **21**, 3583

Simultaneous biochemical and functional phenotyping of single circulating tumor cells using ultrahigh throughput and recovery microfluidic devices†

Yang Liu, [a] Wujun Zhao,[b] Rui Cheng,[c] Jamie Hodgson,[d] Mary Egan,[d] Christen N. Cooper Pope,[d] Petros G. Nikolinakos[d] and Leidong Mao *[c]

Received 24th May 2021,
Accepted 24th July 2021

DOI: 10.1039/d1lc00454a

rsc.li/loc

Profiling circulating tumour cells (CTCs) in cancer patients' blood samples is critical to understand the complex and dynamic nature of metastasis. This task is challenged by the fact that CTCs are not only extremely rare in circulation but also highly heterogeneous in their molecular programs and cellular functions. Here we report a combinational approach for the simultaneous biochemical and functional phenotyping of patient-derived CTCs, using an integrated inertial ferrohydrodynamic cell separation (i^2FCS) method and a single-cell microfluidic migration assay. This combinatorial approach offers unique capability to profile CTCs on the basis of their surface expression and migratory characteristics. We achieve this using the i^2FCS method that successfully processes whole blood samples in a tumor cell marker and size agnostic manner. The i^2FCS method enables an ultrahigh blood sample processing throughput of up to 2×10^5 cells s^{-1} with a blood sample flow rate of 60 mL h^{-1}. Its short processing time (10 minutes for a 10 mL sample), together with a close-to-complete CTC recovery (99.70% recovery rate) and a low WBC contamination (4.07-log depletion rate by removing 99.992% of leukocytes), results in adequate and functional CTCs for subsequent studies in the single-cell migration device. For the first time, we employ this new approach to query CTCs with single-cell resolution in accordance with their expression of phenotypic surface markers and migration properties, revealing the dynamic phenotypes and the existence of a high-motility subpopulation of CTCs in blood samples from metastatic lung cancer patients. This method could be adopted to study the biological and clinical value of invasive CTC phenotypes.

Introduction

Circulating tumor cells (CTCs) are implicated in the formation of metastatic tumors, which is responsible for as much as 90% of cancer-related mortality.[1–6] While the number of tumor cells in blood circulation correlates to clinical outcomes,[7–9] it has become clear that enumeration alone is not sufficient in understanding their multifaceted role in metastasis, in which CTCs participate in nearly all aspects of the process.[3,10,11] Cancer patients have CTCs of varying phenotypes in their blood circulation;[1,4,10,12–15] while some cells passively detach themselves from the primary tumor,[16] a fraction of them gains the ability to actively invade distant organs through modifying their cellular programs, morphology and surrounding tissues.[17] Cells of this invasive phenotype often exhibit a high-motility trait that allows them to be efficient in hematological spread, thus possessing the greatest threat of metastasis.[3,10,11,18,19] Despite rapid advances in the understanding of the molecular mechanisms of CTCs,[4,13,15] the functional properties of the invasive CTC phenotype remain poorly understood due to the limitations of existing CTC isolation and phenotyping methods.[20–22]

The extreme scarcity of CTCs in blood circulation (<10 CTCs per one milliliter of whole blood) and the lack of methods for the isolation of adequate and functional cells are the main bottlenecks in studying the invasive phenotypes of CTCs.[20,22] CTCs are highly heterogeneous in their biological and biophysical characteristics with multiple phenotypes co-existing, which can evolve dynamically over the course of metastasis.[3,10,11] The existing isolation techniques relying on the expression of tumor cell surface epitopes bias the sampling population and reduce the heterogeneity of captured cells.[20] These techniques also lead

[a] *Department of Chemistry, The University of Georgia, Athens, Georgia, USA*
[b] *FCS Technology, LLC, Athens, GA, 30606, USA*
[c] *School of Electrical and Computer Engineering, College of Engineering, The University of Georgia, Athens, Georgia, USA. E-mail: mao@uga.edu*
[d] *University Cancer & Blood Center, LLC, Athens, GA, 30607, USA*

† Electronic supplementary information (ESI) available. See DOI: 10.1039/d1lc00454a

to immobilized and non-functional CTCs and limit the possibility of conducting functional studies.[20] Physical property separation methods relying on size-based selection can separate larger CTCs from smaller leukocytes without using specific molecular markers for selection. However, the isolated cells are contaminated with a large number of leukocytes and may also miss CTCs that are morphologically similar to the leukocytes. As such, the current microfluidic methods for invasiveness phenotyping of tumor cells are mostly confined to cultured cancer cells rather than patient-derived CTCs.[23–27] New methods are thus needed to isolate adequate and functional CTCs from patient samples so that the properties of invasive cells can be identified.

Here we report a novel combinational approach, which first uses an integrated inertial ferrohydrodynamic cell separation (i^2FCS) method to recover all CTCs from blood samples with minimal contamination in a tumor cell marker and size agnostic manner. Adequate and functional CTCs isolated from

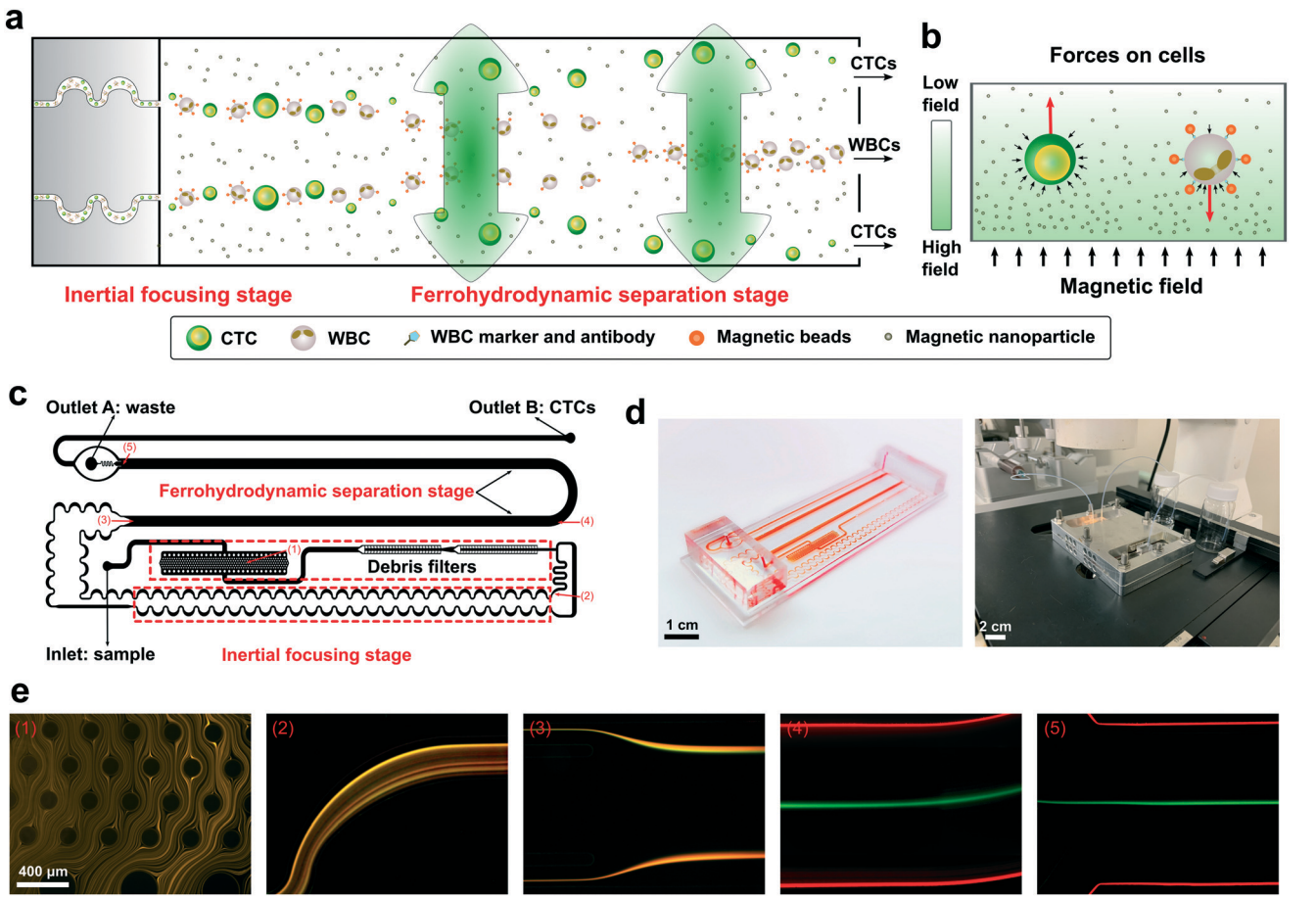

Fig. 1 Overview of the integrated inertial ferrohydrodynamic cell separation (i^2FCS) scheme and its device. (a) Two stages (inertial focusing and ferrohydrodynamic separation) are integrated into the i^2FCS device. The first inertial focusing stage focuses suspended cells in the ferrofluid into a narrow stream in sigmoidal microchannels with alternating curvatures. The second ferrohydrodynamic separation stage directs unlabeled CTCs toward the upper and lower locations of the channel, and WBCs toward the center of the channel, using a symmetric magnetic field distribution with its maximum aligned to the channel center from a sextupole magnet array. Arrows indicate the gradient of the magnetic field. (b) Schematic illustration of circulating tumor cells (CTCs) experiencing "diamagnetophoresis" and labeled white blood cells (WBCs) experiencing both "diamagnetophoresis" and "magnetophoresis" in a colloidal magnetic nanoparticle suspension (ferrofluid). Unlabeled CTCs with close to zero magnetization experience magnetic buoyancy under an external magnetic field, which is generated by the magnetic nanoparticle-induced pressure imbalance on the cell's surface, and is proportional to the cell's volume. This force moves the CTCs toward the minimum of a non-uniform magnetic field. Magnetic bead labeled WBCs experience both "diamagnetophoresis" from the cell surface and "magnetophoresis" from the attached beads in a ferrofluid and move towards the maximum of the magnetic field because the magnetophoretic effect outweighs the diamagnetophoretic effect. The color bar indicates the relative amplitude of the magnetic field. Red arrows show the direction of the cell movement, and small black arrows on the cell surface show the direction of magnetic nanoparticle induced surface pressure on cells. (c) Top view of the i^2FCS device. Cells are injected into the sample inlet and purified with debris filters to remove debris larger than 60 μm. After being inertially focused in the inertial focusing stage, cells of different magnetization were separated in the ferrohydrodynamic separation stage. (d) A photo of the i^2FCS device microchannel (left) and assembled i^2FCS device with sextupole magnets inside an aluminum holder (right). (e) Images of the i^2FCS device in operation. Red (15 μm diameter) diamagnetic polystyrene beads and green (11.8 μm diameter) magnetic polystyrene beads were mixed in a ferrofluid and injected into the device for imaging: (1) particles in the debris filter; (2) particles prior to the inertial focusing stage; (3) particles after inertial focusing; (4–5) particles in the ferrohydrodynamic separation stage. The sample flow rate in this experiment was 500 μL min^{-1} (30 mL h^{-1}).

this method enable their biochemical and functional properties to be quantitatively profiled using a microfluidic assay that can track a single tumor cell's chemotactic migration over time. In isolating CTCs when they are present at extremely low levels in whole blood, we find that the i^{2}FCS method enables an ultrahigh blood sample processing throughput of up to 2×10^5 cells s^{-1} with a sample flow rate of 60 mL h^{-1}, resulting in a device processing time of 10 minutes for a standard 10 mL blood sample. The short processing time, together with a close-to-complete CTC recovery rate of 99.70% and a low WBC contamination of ~507 WBC carryover per milliliter blood processed, preserves the isolated CTCs' viability and biological functions, allowing simultaneous biochemical and functional phenotyping of single tumor cells isolated from cancer patients' blood. Using this approach, we reveal a great diversity of biochemical and functional phenotypes of CTCs with single-cell resolution. CTCs with different levels of epithelial and mesenchymal marker expression exhibit varying chemotactic migration profiles, and there exists a high-motility subpopulation of CTCs in the patients' samples.

Results and discussion

Overview of the i^{2}FCS approach

The integrated inertial ferrohydrodynamic cell separation (i^{2}FCS) approach leverages the integration of cell size-based inertial focusing and cell magnetization-based ferrohydrodynamic separation (Fig. 1a) for tumor cell marker and size agnostic isolation. In this approach, a mixture of a red blood cell lysed blood sample from cancer patients and a colloidally stable magnetic fluid (ferrofluid) first flows through an inertial focusing stage, in which both tumor cells and blood cells are ordered into narrow streams in sigmoidal microchannels with alternating curvatures. The channel geometry and flow parameters in this stage enable the cells to experience inertial lift and Dean drag that force them to migrate to balanced locations within the curved channel (Fig. 1a and e).[28–30] In the second stage of the approach, inertially focused cell streams are ferrohydrodynamically separated into different spatial locations according to their magnetization difference. Its physical principle, illustrated in Fig. 1b, shows that white blood cells (WBCs) are rendered magnetic by labeling of magnetic microbeads through a combination of leukocyte biomarkers, while CTCs remain unlabeled. The magnetization of the ferrofluid is fine-tuned to be less than that of the WBC–bead conjugates, so that unlabeled CTCs with close to zero magnetization, regardless of their size profiles, are collected *via* a magnetic field minimum close to the boundary regions of the microchannel due to a phenomenon known as "diamagnetophoresis",[31] while the WBC–bead conjugates are depleted *via* a magnetic field maximum at the channel center through a competition between both "magnetophoresis" and "diamagnetophoresis" (Fig. 1e). The integration of inertial focusing and ferrohydrodynamic separation results in a compact microfluidic device with just one fluidic inlet and two fluidic outlets (Fig. 1c), which can be operated using a single syringe pump for CTC isolation (Fig. 1d).

Design principles of the i^{2}FCS approach

The i^{2}FCS approach was optimized to realize isolation of functional CTCs in a tumor cell marker and size agnostic manner. The optimized i^{2}FCS device has the following characteristics: (1) complete isolation of CTCs from blood samples with a 99.70% recovery rate; (2) an ultrahigh throughput of >600 million nucleated cells per hour (up to 200 000 cells s^{-1}) and an ultrahigh sample flow rate of 60 mL h^{-1}; (3) an extremely low carryover of ~507 WBCs for every 1 mL of blood processed; (4) isolated CTCs preserving their initial viability and functions and enabling their biochemical and functional analysis. These performance characteristics were realized through optimizing the i^{2}FCS device's geometry, magnetic field pattern, WBC functionalization, sample flow rate and ferrofluid concentration. A physical model that could predict the dynamics of cells in the i^{2}FCS device was developed for the optimization process.[32,33]

Firstly, the channel dimensions of both inertial focusing and ferrohydrodynamic separation stages in i^{2}FCS were designed to accommodate a high blood sample flow of 60 mL h^{-1}, which greatly reduced the device processing time of the blood samples (10 minutes for a standard 10 mL blood sample). For the inertial focusing stage, we designed it so that both tumor and blood cells with diameters larger than 4 μm could be efficiently focused at a flow rate of 60 mL h^{-1}. The geometry of the inertial focusing stage was fine-tuned so that the particle Reynolds number (R_p) was 5.4 and the channel Reynolds number (R_c) was 51.5 when the flow rate was 60 mL h^{-1}, ensuring a well-focused cell stream (~100 μm in width) before the ferrohydrodynamic separation stage. For the ferrohydrodynamic separation stage, the channel dimensions (54.8 × 1.2 × 0.06 mm, length × width × height) were optimized so that the channel Reynolds number was 21.3 when the sample flow rate was 60 mL h^{-1}, ensuring unperturbed laminar flow conditions during CTC isolation. Secondly, we designed the generation of magnetic fields in i^{2}FCS with a sextupole magnet configuration (Fig. 2) to obtain a significant magnetic force on the cells for efficient cell separation. A magnetic flux density of up to 3.2 T (1.1–1.4 T within the ferrohydrodynamic separation channel) (Fig. 2a–d) and a gradient of magnetic flux of up to 670 T m^{-1} (Fig. 2e) were obtained from the sextupole configuration. As shown in Fig. 2b and d, the magnetic flux density was maximal at the center of the separation microchannel, while the absolute value of the flux density gradient was minimal. Using this magnetic field pattern, the directions of the magnetophoretic WBCs and diamagnetophoretic CTCs in the microchannel are opposite to each other, eliminating the need for sheath flow in the i^{2}FCS device and simplifying the device's fluidic operation. Thirdly, we optimized the WBC functionalization by using a combination of five leukocyte biomarkers (CD45, CD45RA, CD66b, CD16, and CD3).[34] Biotinylated biomarker

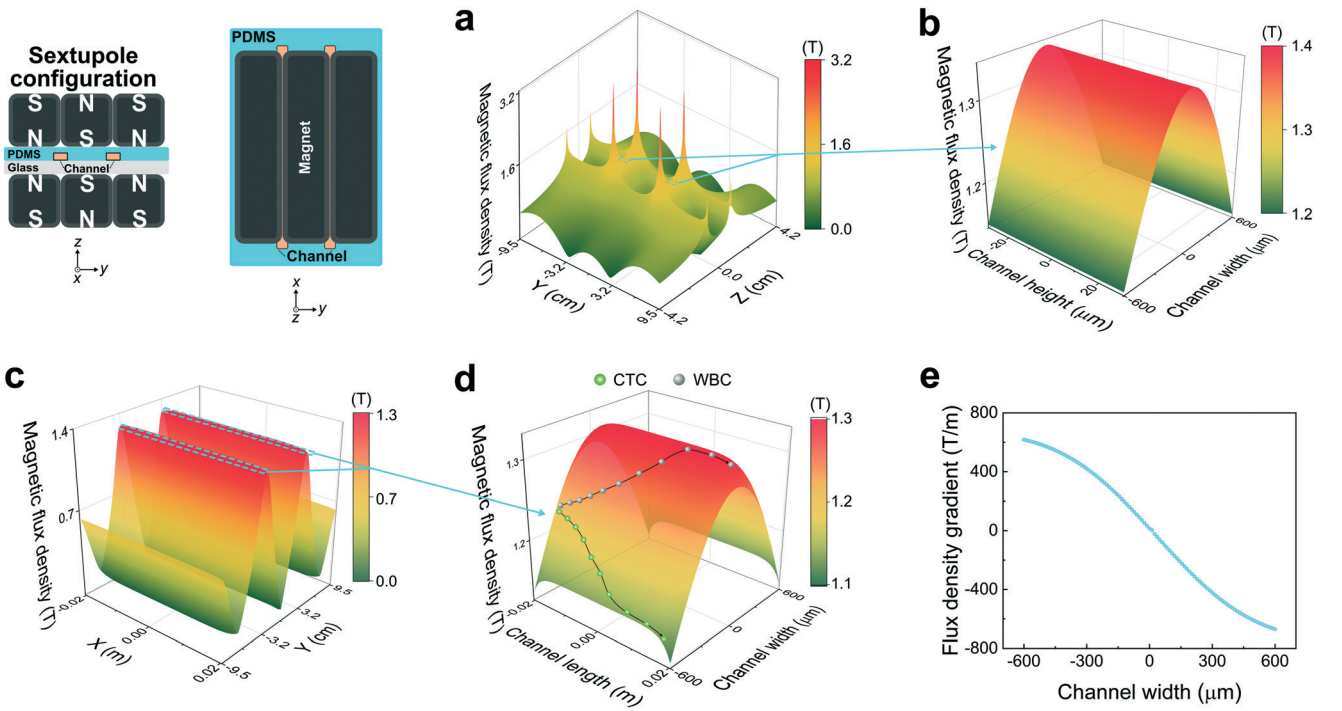

Fig. 2 Optimization of the magnetic field to achieve high magnetic flux density and flux density gradient in the i^{2}FCS device. Six neodymium permanent magnets (each with dimensions of L × W × H, 50.8 × 6.35 × 6.35 mm) were arranged in a sextupole configuration in the i^{2}FCS device. (a) Distribution of the magnetic flux density of the sextupole magnet array in the *y*–*z* plane (*x* = 0). Microfluidic channels were placed between the junctions of the magnets. (b) A symmetric magnetic field was generated in the i^{2}FCS device channel with the highest magnetic flux density located at the center of the microchannel in the *y*–*z* plane (*x* = 0). (c) Distribution of the magnetic flux density of the magnet array in the *x*–*y* plane (*z* = 0). Microchannels (cyan dashed lines) were placed in the area with the highest magnetic flux density in a symmetric pattern. (d) Diamagnetic CTCs (green) moved to the area with a minimal magnetic field while magnetically labeled WBCs (gray) moved to the area with a maximal magnetic field in the i^{2}FCS device channel. (e) Distributions of the magnetic flux density gradient in the microchannel. A magnetic flux density gradient of 670 T m^{-1} in the *y*–*z* plane (*x* = 0) was located near the edge of the channel.

antibodies were labeled with the WBCs and then conjugated with streptavidin-coated Dynabeads (1.05 μm diameter, 11.4% volume fraction of magnetic materials). The use of five markers allowed us to reduce the number of Dynabeads per WBC (20 per cell), because on average, streptavidin-coated Dynabeads had a high probability of conjugating to WBCs due to the increased presence of biotins from the five markers. In our experience, unconjugated Dynabeads tended to clog microchannels under strong magnetic field gradients. Therefore, the decreased use of Dynabeads in this method resulted in the elimination of microchannel clogging issues. With this labeling protocol, WBCs were conjugated with 21 ± 9 (mean ± s.d.) beads and >99.95% of WBCs were labeled with at least two beads (Fig. 3a, left). Based on the number of beads on the WBCs and the corresponding cell size, we calculated the upper bound of the magnetic volume fraction of the ferrofluid to deplete WBCs. Lastly, we studied the effects of the ferrofluid concentration and blood sample flow rate on the separation performance in the above-mentioned physical model. The simulated cell position (denoted as *Y*) and separation distance between WBCs and tumor cells at the device outlets (denoted as Δ*Y*) against the ferrofluid concentration and sample flow rate are shown in Fig. 3c and d. The maximal separation distance was observed when the ferrofluid concentration was 0.015% (Fig. 3c) and the flow rate was 1000 μL min^{-1} or 60 mL h^{-1} (Fig. 3d). Using these optimized parameters (ferrofluid concentration: 0.015% (v/v); flow rate: 1000 μL min^{-1} or 60 mL h^{-1}), the positions of 10 000 MCF7 cancer cells and 10 000 labeled WBCs at the outlets of the device were simulated and are shown in Fig. 3e. 100% of the MCF7 breast cancer cells are deflected toward the channel walls and are collected from the CTC outlet of the device (Fig. 3f), while approximately 99.95% of the WBCs are depleted through the WBC outlet (Fig. 3g).

Throughput, recovery, purity and biocompatibility of the i^{2}FCS approach

Using the optimized i^{2}FCS device and operating parameters, we validated it with spiked cancer cells from a total of 11 cultured cancer cell lines, including 4 breast cancer cell lines (MCF7, MDA-MB-231, HCC1806, HCC70), 4 non-small cell lung cancer cell lines (A549, H1299, H3122, H520), 2 small cell lung cancer cell lines (DMS79, H69), and 1 prostate cancer cell line (PC-3). We evaluated the performance of i^{2}FCS in the cancer cell isolation, including the sample flow rate and cell-processing throughput, cell recovery rate, WBC contamination, viability and proliferation of isolated cells.

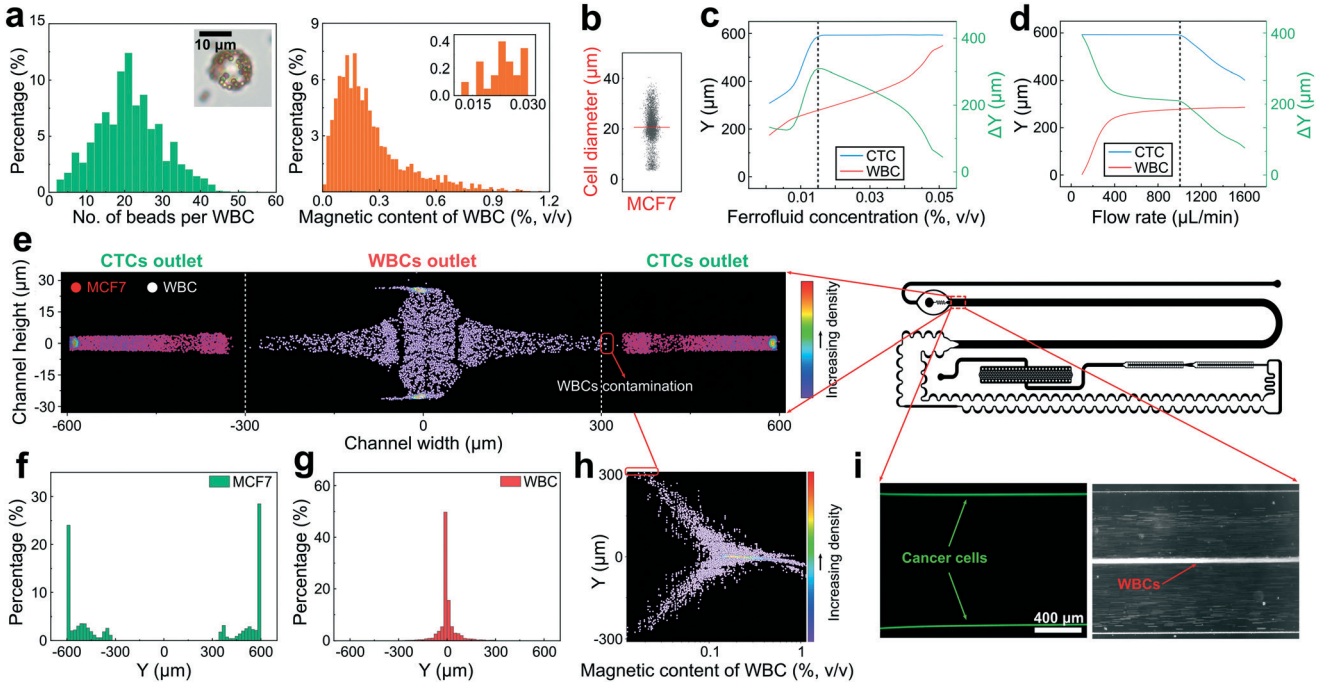

Fig. 3 System optimization of the i^{2}FCS device for the isolation of CTCs (down to 10 cells per mL) with a high recovery rate, low WBC contamination, and ultrahigh throughput. (a) Optimization of magnetic bead labeling of WBCs. Left: distribution of the number of magnetic beads labeled on WBCs (n = 2000). On average, there are 21 ± 9 (mean ± s.d.) Dynabeads conjugated onto a single WBC. More than 99.95% of WBCs are labeled with at least two beads. The inset is a WBC labeled with multiple Dynabeads. Right: distribution of the magnetic content in labeled WBCs. More than 99.9% of WBCs have a volume fraction of magnetic content larger than 0.015% (v/v). (b) Effective diameter distribution of the human breast cancer cell line (MCF7). Its diameter is 20.6 ± 6.6 μm (mean ± s.d., n = 5000). (c and d) Optimization of the ferrofluid concentration and flow rate for i^{2}FCS to achieve the maximal separation distance (ΔY) between CTCs and WBCs. The optimized ferrofluid concentration is 0.015%, while the flow rate is 1000 μL min^{-1} (60 mL h^{-1}). During the optimization, the magnetic flux density and its gradient are the same as in Fig. 2. (e) Simulation of cell distributions at the cross-section of the outlet of the i^{2}FCS device. 10 000 MCF7 cells and 10 000 labeled WBCs were used to mimic the heterogeneity of the blood sample. After device processing, 100% of CTCs are collected from the CTC outlet with 0.05% (5 of 10 000) WBC contamination. 99.95% of WBCs are depleted from the WBC outlet. MCF7 cancer cells are represented with red dots and WBCs are represented with white dots. The color of the edges of the dots represents the density of the cells at that location. (f and g) Quantification of CTC and WBC distribution at the end of the i^{2}FCS device. (h) Dependence of the final position (Y) of WBCs along the channel width at the outlet of the device on the magnetic content of individual WBCs. Simulation parameters of e–h include a ferrofluid concentration of 0.015% and a sample flow rate of 1000 μL min^{-1} (60 mL h^{-1}). (i) Visualization of cancer cell isolation and WBC depletion (left: epifluorescence; right: bright field). Diamagnetic cancer cells were collected from the top and bottom outlets while the WBCs labeled with magnetic beads were depleted from the middle outlet. The cells were suspended in 0.015% ferrofluid and processed with a flow rate of 1000 μL min^{-1} (60 mL h^{-1}).

Fig. 3i shows a typical separation process, in which ~100 MCF7 breast cancer cells stained with green fluorescence were spiked into 1 mL of WBCs (~6 million cells per mL) and processed at a flow rate of 60 mL h^{-1}. The cancer cells and WBCs were distinctively separated into different streams at the outlets of the device. No channel clogging due to magnetic beads was observed during the device operation processing up to 600 million nucleated cells with a throughput of 100 000 cells s^{-1} and a flow rate of 60 mL h^{-1}. The throughput and flow rate of i^{2}FCS are approximately one order of magnitude higher than those of most existing CTC isolation methods (see the ESI†). The ultrahigh throughput of i^{2}FCS enables processing a typical blood sample of 10 mL in 10 minutes, significantly reducing chances of cell apoptosis during the device operation. We further evaluated the performance of i^{2}FCS in recovering spiked cancer cells at clinical concentrations (10–200 cells mL^{-1}). MCF7 breast cancer cells with spike ratios ranging from 10 to 200 cells per mL were recovered using the device at a recovery rate of 100% with minimal variations (n = 3, Fig. 4a), indicating the ability of i^{2}FCS to completely recover spiked cancer cells at clinical concentrations. We further challenged the device with 10 additional cancer cell lines with distinct size profiles (Fig. 4b). i^{2}FCS showed close-to-complete recovery rates across all cancer cell lines used in this study (100.00 ± 0.00%, 99.33 ± 0.49%, 99.67 ± 0.47%, 99.83 ± 0.24%, 99.67 ± 0.47%, 99.67 ± 0.42%, 100 ± 0.00%, 100 ± 0.00%, 100 ± 0.00%, 99.67 ± 0.94%, and 98.83 ± 1.03% for MCF7, MDA-MB-231, HCC1806, HCC70, A549, H1299, H3122, H520, DMS79, H69, and PC-3 cell lines, mean ± s.d., n = 3 for each cell line) (Fig. 4c). The average recovery rate across the 11 cancer cell lines was 99.70 ± 0.34% (mean ± s.d., n = 11), including the small cell lung cancer cells (DMS79 and H69). The recovery rate of the i^{2}FCS device is higher than those of other microfluidic approaches (see the ESI†), including the CTC-iChip.[35,36] The current range of cell concentration processed

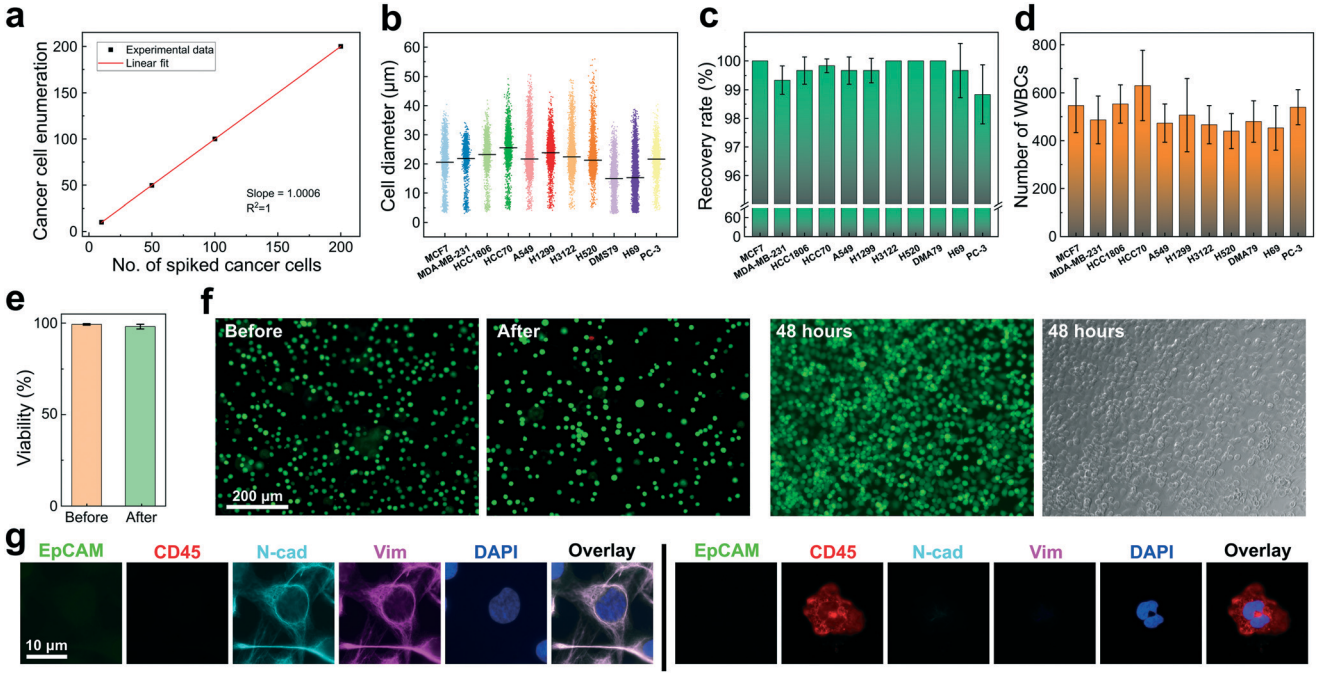

Fig. 4 Characterization of the i²FCS device performance using cancer cell lines spiked into blood from healthy donors. Cancer cells and WBCs were processed in 0.015% (v/v) ferrofluid with a flow rate of 1000 μL min^{-1} (60 mL h^{-1}) to achieve a high cancer cell recovery rate and low WBC contamination. (a) Spike-in experiments indicated a high recovery rate (100%) of cancer cells. Experiments with different numbers (10, 50, 100, and 200) of MCF7 cells spiked into 1 mL of labeled WBCs. An average recovery rate of 100% was achieved (R^2 = 1, n = 3). (b) Diameter distribution of 11 cancer cell lines. (c) Recovery rates of spiked cancer cells (~100 cells per mL, total: 15 mL). Recovery rates of 100.00 ± 0.00%, 99.33 ± 0.49%, 99.67 ± 0.47%, 99.83 ± 0.24%, 99.67 ± 0.47%, 99.67 ± 0.42%, 100 ± 0.00%, 100 ± 0.00%, 100 ± 0.00%, 99.67 ± 0.94%, and 98.83 ± 1.03% were achieved for MCF7 (breast cancer), MDA-MB-231 (breast cancer), HCC1806 (breast cancer), HCC70 (breast cancer), A549 (non-small cell lung cancer), H1299 (non-small cell lung cancer), H3122 (non-small cell lung cancer), H520 (non-small cell lung cancer), DMS79 (small cell lung cancer), H69 (small cell lung cancer), and PC-3 (prostate cancer) cell lines, respectively (mean ± s.d., n = 3). (d) The corresponding WBC contaminations for each cell line are 547 ± 113, 487 ± 100, 553 ± 80, 630 ± 147, 473 ± 80, 507 ± 153, 467 ± 82, 440 ± 73, 480 ± 87, 453 ± 93, and 540 ± 73 WBCs per mL blood (mean ± s.d., n = 3). (e) Short term viability of H1299 lung cancer cells before and after i²FCS processing was determined to be 99.31 ± 0.42% (mean ± s.d., n = 3) and 98.10 ± 1.35% (mean ± s.d., n = 3), respectively. (f) Images of live/dead staining before and after enrichment, and long-term (48 hours) proliferation test. The cells were stained with Calcein AM (green, live cells) and EhD-1 (red, dead cells). (g) Immunofluorescence images of H1299 lung cancer cells and WBC contamination after enrichment. Five channels including EpCAM (green), CD45 (red), N-cadherin (N-Cad, cyan), vimentin (Vim, magenta), and DAPI (blue) were used.

by i²FCS was 3–20 million cells per mL. Higher cellular concentration would slightly decrease the cancer cell recovery rate (see the ESI†). i²FCS also greatly reduced the contamination of WBCs. The i²FCS device achieved 4.07-log depletion of WBCs by removing 99.992% of the leukocytes from the blood samples, with approximately 507 ± 53 (mean ± s.d., n = 3) cell carryover in the CTC collection outlet after processing 1 mL of blood (Fig. 4d). The majority of contaminating WBCs were WBCs labeled with ≤1 magnetic bead. The level of WBC contamination found in the i²FCS device is significantly lower than those in the majority of other microfluidic approaches (see the ESI†), and is comparable to that of the CTC-iChip approach.[35,36] Lastly, we investigated the effect of the device processing on the cells' viability and proliferation. The combination of low ferrofluid concentration (0.015% magnetic content by volume) and laminar flow conditions in the i²FCS device showed little impact on the viability, intactness and proliferation of the isolated cancer cells. Fig. 4e shows that the cell viabilities of H1299 lung cancer cells before and after i²FCS processing were 99.31 ± 0.42% and 98.10 ± 1.35% (mean ± s.d., n = 3), respectively, indicating a negligible device effect on the cell viability. The fluorescence images of the live/dead assay in Fig. 4f show that the viability and intactness of the cancer cells were well preserved after the device processing. The isolated cancer cells continued to proliferate to confluence after 48 hours of culture (Fig. 4f), with unaffected marker expression on their surface (Fig. 4g).

Biochemical phenotyping of CTCs in cancer patients

To evaluate the performance of i²FCS in isolating heterogeneous CTCs in clinical samples, we conducted a study of samples collected from 2 patients exhibiting stage IV metastatic non-small cell lung cancer. Immunofluorescence staining was used to distinguish CTCs and WBCs, and CTCs of different phenotypes. We used the i²FCS device to process the blood samples from the patients, who were recruited and gave informed consent at the University Cancer and Blood Center (Athens, Georgia) under an approved IRB protocol

(University of Georgia, VERSION00000869). Surface markers corresponding to epithelial and mesenchymal phenotypes were chosen because CTCs are reported to go through EMT, epithelial to mesenchymal transition, in which the original epithelial tumor cells transition into stem-like mesenchymal cells.[10,11,37] The loss of epithelial characteristics and the acquisition of mesenchymal characteristics are closely linked to the tumor cells' high motility and invasiveness to create a new tumor site.[10,37–39] CTCs of this functional phenotype are therefore the focus of this study. 20 mL of blood sample from each patient was processed by the i^{2}FCS device. A quarter of the isolated cells were used for biochemical phenotyping through immunofluorescence staining with an epithelial marker (EpCAM) that is downregulated in EMT,[20,37,38] two mesenchymal markers (vimentin and N-cadherin) that are upregulated in EMT,[18,37,38] a leukocyte marker (CD45), and a nucleus marker (DAPI) for their identification. WBCs were identified as CD45 positive and DAPI positive (EpCAM−/Vim−/N-cad−/CD45+/DAPI+). The CD45 negative and DAPI positive CTCs were classified into three different phenotypes including the epithelial phenotype (EpCAM+/Vim−/N-cad−), mesenchymal phenotype (EpCAM−/Vim+/N-cad−, EpCAM−/

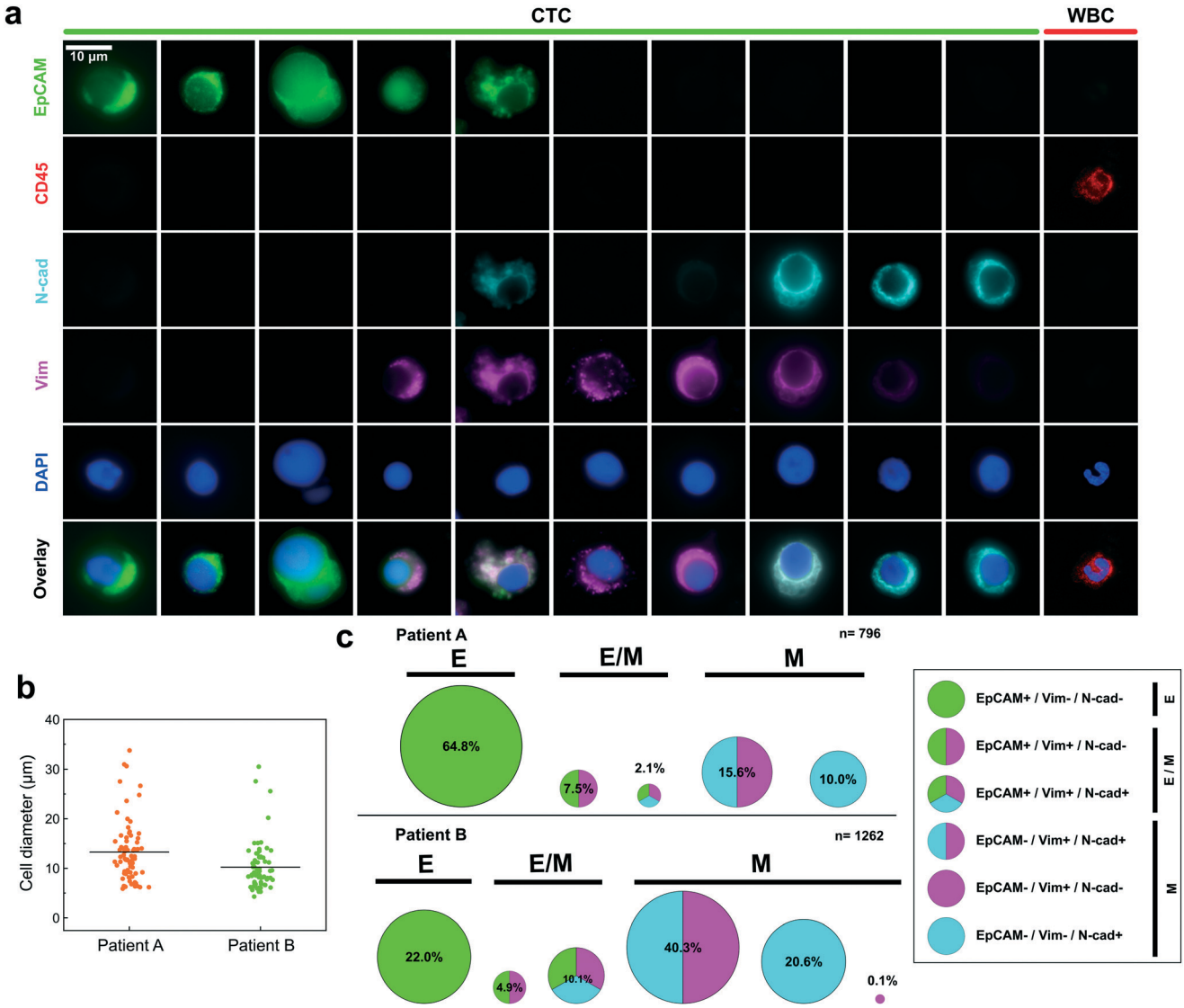

Fig. 5 Biochemical phenotyping of CTCs isolated from two metastatic lung cancer patients (n = 2). (a) Immunofluorescence images of 11 selected CTCs and 1 WBC from the two patients. Five channels were used in the immunofluorescence staining including epithelial CTC marker EpCAM (green), leukocyte marker CD45 (red), mesenchymal CTC markers N-cadherin (N-Cad, cyan) and vimentin (Vim, magenta), and nucleus marker DAPI (blue). Cells were identified to be either epithelial positive (EpCAM+/CD45−/DAPI+), mesenchymal positive (N-cad+/CD45−/DAPI, Vim+/CD45−/DAPI+, and N-cad+/Vim+/CD45−/DAPI+), or mixed epithelial and mesenchymal positive (EpCAM+/N-Cad+/Vim+/CD45−/DAPI). (b) Statistical analysis of cell diameters of collected CTCs from the patients. CTCs from patient A (lung cancer, stage IV) had a diameter of 13.29 ± 6.13 μm (mean ± s.d., n = 75); CTCs from patient B (lung cancer, stage IV) had a diameter of 10.22 ± 4.85 μm (mean ± s.d., n = 70). (c) Quantitative analysis of surface antigen expression of individual CTCs from the patients. Epithelial positive CTCs (E) were identified as EpCAM+/Vim−/N-cad−. Mixed epithelial and mesenchymal CTCs (E/M) were identified as EpCAM+/Vim+/N-cad− and EpCAM+/Vim+/N-cad+. Mesenchymal CTCs (M) were identified as EpCAM−/Vim+/N-cad+, EpCAM−/Vim+/N-cad−, and EpCAM−/Vim−/N-cad+.

Vim−/N-cad+, or EpCAM−/Vim+/N-cad+), and mixed epithelial and mesenchymal phenotypes (EpCAM+/Vim+/N-cad− or EpCAM+/Vim+/N-cad+).

Examples of isolated CTCs are shown in Fig. 5a. We first note that a significant number of CTCs were isolated from both patients' blood samples. 796 cells were identified as CTCs from patient A in a 5 mL volume of blood sample at a concentration of 159 CTCs per mL of blood sample, and 1262 were identified in patient B's sample (5 mL blood, 252 CTCs per mL concentration). The high counts of CTCs could be explained by the disease stages (stage IV metastatic non-small cell lung cancers) of both patients and the ability of i^{2}FCS to completely recover CTCs from blood. For verification purposes, a blood sample from a third patient (patient C, stage IV lung cancer) was processed by both i^{2}FCS and a recently reported size-selection method (inertial-FCS),[40] both of which yielded similarly high counts of CTCs (see the ESI†). The isolated CTCs from both patients were intact, indicating a minimal impact of the device processing on the cell morphology. Consistent with previous reports,[32,41–46] the effective cell diameter of isolated CTCs, defined as the maximum Feret diameter of the cells under bright-field imaging, showed a high level of variation for both patients. The effective diameters of randomly selected (n = 75) CTCs from patient A's sample were 13.29 ± 6.13 μm (mean ± s.d.), with the smallest diameter being 5.88 μm and the largest being 33.74 μm (Fig. 5b). For patient B, the effective diameters of randomly selected CTCs (n = 70) were 10.22 ± 4.85 μm (mean ± s.d.), where the smallest diameter was 4.28 μm and the largest was 30.51 μm (Fig. 5b). While the clinical relevance of CTCs with varying sizes is unclear, some consider that cells switching from an active state to a dormant state may be the cause of their size variation, which could contribute to their metastatic potential.[43] Nonetheless, the polydispersity of isolated cells highlights the effectiveness of the cell size agnostic i^{2}FCS approach in recovering CTCs that are comparable in size to WBCs, enabling downstream studies on these cells. We further characterized the biochemical phenotypes of the isolated CTCs through their surface antigen expression using the above-mentioned epithelial and mesenchymal markers. The proportion of each of the phenotypic subtypes of CTCs is summarized in Fig. 5c, which shows an interesting comparison between the two patients. The isolated CTCs of patient A had a significant portion of the epithelial phenotype (64.8% EpCAM+/Vim−/N-cad−) while patient B's CTCs had a predominant portion of the mesenchymal phenotype (40.3% EpCAM−/Vim+/N-cad+, 20.6% EpCAM−/Vim−/N-cad+, and 0.1% EpCAM−/Vim+/N-cad−), indicating that the majority of patient B's cells have gone through the EMT. Patient A also presented 25.6% mesenchymal CTCs (15.6% EpCAM−/Vim+/N-cad+ and 10.0% EpCAM−/Vim−/N-cad+) in addition to the epithelial phenotype. Patient B presented 22.0% epithelial CTCs (EpCAM−/Vim+/ N-cad) in addition to the mesenchymal phenotype. Both patients had a relatively small percentage of CTCs that presented mixed epithelial and mesenchymal phenotypes (patient A: 7.5% EpCAM+/Vim+/N-cad− and 2.1% EpCAM+/Vim+/N-cad+; patient B: 4.9% EpCAM+/Vim+/N-cad− and 10.1% EpCAM+/Vim+/N-cad+, Fig. 5c). The cells with mixed epithelial and mesenchymal phenotypes likely represented CTCs that were in transition between epithelial and mesenchymal states, indicating their evolution to more invasive phenotypes. Overall, the heterogeneity of biomarker expression of isolated CTCs from these patients is consistent with previous reports and highlights the marker agnostic isolation of the i^{2}FCS approach. CTCs of the mesenchymal phenotype are reported to exhibit high motility and are more invasive than those of the epithelial phenotype.[10,37–39] Therefore identifying the invasive subtype of CTCs with high motility is the focus of the subsequent functional study.

Functional phenotyping of CTCs in cancer patients

Adequate and functional CTCs isolated from the i^{2}FCS approach enable their simultaneous biochemical and functional phenotyping. In this study, we assessed how subpopulations of CTCs with different levels of epithelial and mesenchymal marker expression affect their chemotactic migration. We chose cell migration to assess CTCs' functions because the high motility of these cells is implicated in the metastatic spread, including local invasion into the surrounding stroma and intravasation into blood circulation, extravasation into the parenchyma of foreign tissue, colonization and formation of metastatic lesions.[3,10,11,18,19] The identification of high-motility CTCs would facilitate the prediction of a patient's risk of developing metastasis and the design of personalized therapeutics. The ultrahigh recovery rate of i^{2}FCS allows us to isolate all CTCs from the patient samples, which potentially contain a subpopulation of these highly motile CTCs. In order to identify this subpopulation, we developed a new microfluidic assay that tracked cell chemotactic migration with single cell resolution over a 24 hour period in confined microchannels.

The CTC isolation and migration characterization process is shown in Fig. 6a. 20 mL of blood sample from patient B was first processed by the i^{2}FCS device to isolate CTCs. Patient A's sample experienced a delay in its processing and was not included in the migration study. The isolated cells from patient B were divided into three portions, with one quarter of the cells being used for biochemical phenotyping through immunofluorescence staining (described in the previous section) and one quarter for the microfluidic migration assay. The remaining half of the cells were preserved for future studies. In constructing the microfluidic device and assay for CTC migration phenotyping, we applied the following design principles. Firstly, we chose to use chemotactic migration to guide the CTC migratory direction in the microfluidic assay because CTCs are most efficient when the cells are involved in directed migration.[47,48] We used a spatial gradient of growth factors including epidermal growth factor (EGF), basic fibroblast growth factor (bFGF) and fetal bovine serum (FBS), to guide the CTC migration in the microchannels,[49] and a spatial gradient of

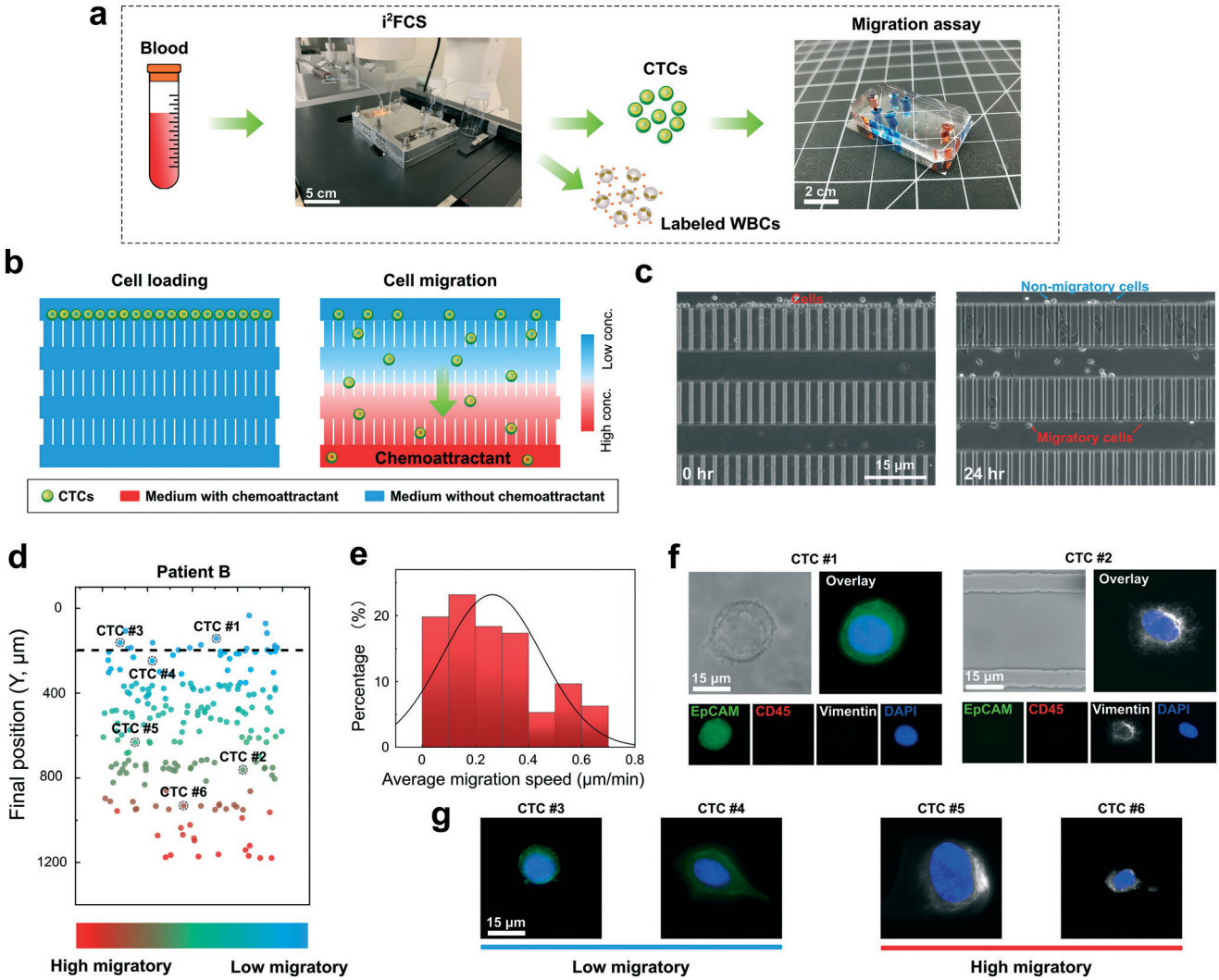

Fig. 6 Functional phenotyping of CTCs isolated from one metastatic lung cancer patient (n = 1). (a) Illustration of the procedure for CTC isolation *via* an i^{2}FCS device, and migration characterization of isolated CTCs *via* a single-cell migration device. 20 mL of patient blood was processed using the i^{2}FCS device. A quarter of isolated cells were used in the single cell migration microfluidic device. (b) Cells were loaded into the top microchannel at the beginning of the migration assay. A gradient of growth factors was established over a 24 hour period *via* continuous perfusion to allow phenotyping of cells with different migratory distances and speeds. The direction of the arrow indicates the gradient of the growth factors. (c) Characterization of the migration device using H1299 lung cancer cells. Bright field images of migrated H1299 cells at the end of the 24 hour period show migratory *versus* non-migratory cell populations. (d) Migration distance of CTCs (n = 207) from patient B's blood sample. Cells were loaded into the migration device at a similar starting position (dashed line, Y = 200 μm). A gradient of growth factors (10% fetal bovine serum, FBS; epidermal growth factor, EGF; and basic fibroblast growth factor, bFGF) was used to guide the migration of CTCs, while a gradient of a chemorepellent (Slit2) was used to inhibit the migration of carryover WBCs. After the 24 hour migration, the cells in the device were immunofluorescently stained with anti-EpCAM (green), anti-CD45 (red), anti-vimentin (white), and DAPI (green) to identify the cell types. CTCs were identified as EpCAM+/CD45−/DAPI+, EpCAM+/Vim+/CD45−/DAPI+, and Vim+/CD45−/DAPI+, while WBCs were identified as EpCAM−/Vim−/CD45+/DAPI+. (e) The migration speed of CTCs from patient B was 0.26 ± 0.19 μm min^{-1} (mean ± s.d., n = 207). (f) Bright field and immunofluorescence images of one non-migratory CTC (left) and one migratory CTC (right) of patient B, with their final migration position circled in (d). (g) Immunofluorescence images of low migratory cells (left, found in the loading channel of the migration device) and high migratory cells (right, found in the migration tracks of the device).

Slit2 to inhibit the migration of carryover WBCs.[50,51] The gradient of growth factors was maintained *via* continuous perfusion for a 24 hour period in the microchannel to enable chemotactic migration of CTCs (Fig. 6b). Secondly, we constructed microchannels to recapitulate the confined space through which tumor cells infiltrate organs *in vivo*.[19,52–54] A total of 5000 single cell migration tracks were packed in the device for CTCs to migrate, with each track having a cross-section of 30 μm (width) by 5 μm (height) and a total length of 1200 μm (Fig. 6b), close to the dimensions of the tunnel-like tracks CTCs encountered in the extracellular matrix (ECM) of the tumor stroma.[19,52–54] The single cell tracks were periodically interrupted to enable collection of migrated cells at the end of the experiments. This assay was first validated using H1299 lung cancer cells to show that it could differentiate migratory *versus* non-migratory subtypes (Fig. 6c). In experiments using patient-

derived CTCs, cells isolated from patient B using an i^{2}FCS device were seeded in the microfluidic migration device at the loading channel, and allowed to migrate along the growth factor gradient for 24 hours under incubation conditions of 37 °C and 5% CO_2. At the end of the 24 hour period, migratory cells were immunofluorescently stained within the device with an epithelial marker (EpCAM), a mesenchymal marker (Vimentin, Vim), a leukocyte marker (CD45) and a nucleus marker (DAPI) to identify their cell types. The migratory distance and speed of each identified CTC (EpCAM+/Vim−/CD45−/DAPI+, EpCAM−/Vim+/CD45−/DAPI+, or EpCAM+/Vim+/CD45−/DAPI+) in the single cell tracks were recorded and analyzed.

We estimated that a total of ~1260 CTCs isolated from 10 mL of blood sample were seeded in the microfluidic migration device at the start of the migration assay. The number of CTCs was calculated from the concentration of 252 CTCs per mL obtained through immunochemistry for patient B's sample. At the end of the 24 hour migration assay, we identified again through immunochemistry that a small percentage of the initial CTCs (16.4%, 207 out of the 1260 seeded cells) remained in the migration device and exhibited chemotactic migration towards the growth factor gradient. The other 83.6% of the CTCs were likely to be apoptotic and washed away by the perfusion within the assay time frame. Fig. 6d–f summarize the distributions of the final migratory position, migration speed and surface marker expression of the high-motility cell subpopulation. The migration speed of individual cells was calculated from the distance migrated (difference between the initial and final positions within the microchannel) within 24 hours. These high-motility cells exhibited variable levels of migration during the 24 hour period, with a mean speed (Fig. 6e) of 0.26 ± 0.19 μm min^{-1} (mean ± s.d., n = 207). This speed indicated that the migratory CTCs likely utilized the mesenchymal locomotion in the microchannels, which was reported to have a speed range of 0.1–1 μm min^{-1}.[55] We also observed that cells with a faster migratory speed and a longer migratory distance tended to have an elongated cell morphology, while cells with a slower migratory speed and a shorter migratory distance had a mostly rounded shape (Fig. 6f and g), consistent with previous findings of mesenchymal migration.[56,57] Through the single-cell migration assay, we identified a subpopulation of CTCs from patient B's sample that exhibited high motility towards the gradient of growth factors. This subtype of high-motility CTCs exhibits different levels of epithelial and mesenchymal marker expression and varying chemotactic migration properties. The identification of these high-motility CTCs could enable further molecular and functional studies on them.

Comparison of i^{2}FCS to existing CTC enrichment methods

We objectively evaluated the i^{2}FCS performance in CTC separation and compared it to existing methods, using four commonly used metrics in calibrating CTC isolation methods, including the cell-processing throughput, CTC recovery rate, WBC contamination or carryover at the device output and integrity of enriched cells. The i^{2}FCS method reported an ultrahigh blood sample processing throughput of up to 2 × 10^5 cells s^{-1} with a blood sample flow rate of 60 mL h^{-1}. It resulted in a close-to-complete recovery of spiked cancer cells (99.70% recovery rate) and an ultralow WBC contamination (4.07-log depletion of leukocytes, removing 99.992% of the leukocytes from the blood samples, with approximately 507 WBC carryover per 1 mL of processed blood). The short processing time of i^{2}FCS (10 minutes for 10 mL of blood) and the complete recovery of CTCs produced adequate, viable and functional cells for subsequent cell-migration studies. We compared the iFCS performance to those of a total of 49 recently published CTC separation methods (see the ESI†) and found that i^{2}FCS had better overall performance with respect to the above-mentioned four metrics than the existing methods.

We also compared the performance of i^{2}FCS to those of two generations of CTC-iChip as shown in Table 1.[35,36] i^{2}FCS had a six times higher blood sample flow rate (60 mL h^{-1} for i^{2}FCS *versus* 10 mL h^{-1} for monolithic CTC-iChip). Both i^{2}FCS and CTC-iChip depleted roughly the same amount of WBCs from the blood samples (507 cells per mL carryover for i^{2}FCS *versus* 445 cells per mL carryover for monolithic CTC-iChip). While the reported cancer cell recovery rates were almost the same for i^{2}FCS and CTC-iChip using spiked cancer cells (99.7% for i^{2}FCS *versus* 99.5% for monolithic CTC-iChip), the recovered CTCs from the patient samples showed different physical diameter ranges, with i^{2}FCS being able to isolate patient CTCs with a broader physical diameter range than CTC-iChip (4.3–33.7 μm for i^{2}FCS *versus* 5.5–27 μm for monolithic CTC-iChip). i^{2}FCS has an advantage of being able to recover small CTCs, because it does not differentiate CTCs and blood cells based on their physical diameters. Instead it uses the contrast of cellular magnetization for separation. This working principle ensured that all CTCs were separated regardless of their diameters. On the other hand, CTC-iChip integrated deterministic lateral displacement (DLD) to deplete red blood cells, inertial focusing to concentrate nucleated cells, and magnetophoresis to separate magnetically labeled CTCs. The size-based DLD stage in CTC-iChip could potentially remove small CTCs of similar size to red blood cells (6–8 μm). This slight selection bias might explain the diameter difference in recovered CTCs between the two methods. Finally, CTC-iChip could process whole blood without lysis while i^{2}FCS needed red blood cell lysis. Even though the cancer cell loss due to the lysis step was demonstrated to be negligibly small (~0.08%) in cancer cell line control experiments,[32] it would be difficult to characterize such a CTC loss in patient samples. In summary, i^{2}FCS had the advantages of a higher cell-processing throughput and sample flow rate and CTC recovery with broader physical diameters, but lacked the ability to process whole blood when compared to CTC-iChip.

Conclusion

We reported an integrated method that allowed for the first time simultaneous biochemical and functional phenotyping of patient-derived single circulating tumor

Table 1 Comparison of the design, operation and performance of CTC isolation between CTC-iChip and i^{2}FCS

Technology	Blood processing throughput (mL h^{-1})	CTC recovery rate (spiked cell lines)	White blood cell (WBC) carryover at device outlets	Recovered patient CTC diameter range	Cell viability (cell lines)	Design and operation	Red blood cell lysis needed?
CTC-iChip[35]	8	~97%	32 000 WBCs per mL	>9 μm	Not reported	Integration of DLD, inertial focusing and magnetophoresis in two devices	No
Monolithic CTC-iChip[36]	~10	~99.5%	445 WBCs per mL	5.5–27 μm	Not reported	Integration of DLD, inertial focusing and magnetophoresis in a single device	No
i^{2}FCS (this paper)	60	99.7%	507 WBCs per mL	4.3–33.7 μm	98.10%	Integration of inertial focusing and ferrohydrodynamic separation in a single device	Yes

cells. The method leveraged an integrated inertial ferrohydrodynamic cell separation (i^{2}FCS) approach for tumor cell marker and size agnostic isolation of CTCs from patient samples. This approach yielded remarkable CTC isolation performance including complete isolation of CTCs from blood samples with a 99.70% recovery rate, an ultrahigh throughput of >600 million nucleated cells per hour, an ultrahigh blood processing flow rate of 60 mL h^{-1}, and an extremely low carryover of ~507 WBCs for every one milliliter of blood processed. Furthermore, the isolated CTCs from i^{2}FCS preserved their functional properties and enabled their biochemical and functional phenotypes to be quantitatively queried *via* a single cell migration assay.

In samples collected from two metastatic lung cancer patients, i^{2}FCS and the migration assay enabled the sensitive profiling of CTCs' heterogeneity according to their surface antigen levels and migration phenotypes. CTCs profiled in the samples collected from the patients revealed that there was a great level of diversity in the phenotypes of CTCs. CTCs exhibited variable levels of epithelial and mesenchymal antigen expression and morphologies, confirming the marker and size agnostic isolation of the approach. The isolated cells were assessed for their motility towards a gradient of growth factors in a migration assay with single-cell resolution, revealing the existence of a high-motility subpopulation of CTCs in one of the patients' samples.

The i^{2}FCS and migration assay approach could be potentially adapted to a variety of applications in cancer research. CTCs isolated from the i^{2}FCS can readily be recovered with preserved intactness and biological functions, therefore facilitating further downstream analysis and culture. This approach allows multiplexed queries of functional CTCs, which makes it possible to analyze CTCs for their complex roles in metastasis. Experiments using this approach can be implemented using a standard syringe pump with microfluidic devices that are straightforward to fabricate and operate, making it relatively easy for laboratory adaptation.

Experimental section

Modeling and simulation

The magnetic field and particle separation performance was simulated and optimized in MATLAB (MathWorks, Natick, MA) using a physical model, which predicted trajectories of cancer cells and labeled WBCs in the microfluidic channel coupled with a sextupole configuration of magnets.[32,33]

Microfluidic device fabrication

The master mold containing the microfluidic structures was fabricated using standard photolithography methods with SU-82025 photoresist (Kayaku Advanced Materials, Westborough, MA). The height of the structures was measured to be 60 μm. A 1 mm thick PDMS layer was prepared with a Sylgard 184 silicone elastomer kit (Ellsworth Adhesives, Germantown, WI) in a 1 : 7 ratio of a cross-linker and base, and cured at 60 °C for 4 hours. After bonding with the inlet and outlet layers (5 mm thick PDMS), the devices were oven baked at 80 °C for 20 minutes followed by baking on a hotplate at 150 °C for 1 hour. The device was placed within a custom aluminum manifold that held six N52 NdFeB permanent magnets (K&J Magnetics, Pipersville, PA) in a sextupole configuration. The magnets had a geometry of 50.8 mm × 6.35 mm × 6.35 mm (L × W × H) and had a remanent magnetization of 1.48 T each. Before each use, the devices were sterilized with 70% ethanol and then primed with 1× PBS supplemented with 0.5% (w/v) BSA and 2 mM EDTA (Thermo Fisher Scientific, Waltham, MA).

Ferrofluid synthesis and characterization

The water-based ferrofluid was a colloidal suspension of maghemite nanoparticles, synthesized by a chemical co-precipitation method following a developed protocol.[58,59] The saturation magnetization (1107 A m^{-1}) and volume fraction of the ferrofluid (0.298%, v/v) were measured using a vibrating sample magnetometer (VSM, MicroSense, Lowell, MA). The viscosity of the ferrofluid (1.7 mPa s^{-1}) was

characterized using a compact rheometer (Anton Paar, Ashland, VA) at room temperature. The diameter and morphology of maghemite nanoparticles were determined to be 10.91 ± 4.87 nm (mean ± s.d.) with a transmission electron microscope (TEM; FEI, Eindhoven, The Netherlands).

Cell culture and preparation

11 human cancer cell lines including four breast cancer cell lines (MCF7, MDA-MB-231, HCC1806, and HCC70), four non-small cell lung cancer (NSCLC) cell lines (A549, H1299, H3122, and H520), two small cell lung cancer (SCLC) cell lines (DMS79 and H59) and one prostate cancer cell line (PC-3) were purchased from ATCC (Manassas, VA). Cell cultures followed the manufacturer's instructions. Breast cancer cell lines MCF7 and MDA-MB-231 were cultured in DMEM (Thermo Fisher Scientific, Waltham, MA) and the other cell lines were cultured in RPMI 1640 medium (Thermo Fisher Scientific, Waltham, MA). The DMEM and RPMI medium were supplemented with 10% (v/v) fetal bovine serum (FBS, Thermo Fisher Scientific, Waltham, MA), 1% (v/v) penicillin/streptomycin solution (Thermo Fisher Scientific, Waltham, MA), and 0.1 mM non-essential amino acid (NEAA, Thermo Fisher Scientific, Waltham, MA). All the cell lines were cultured at 37 °C with 5% CO_2. When the cells were grown to 80% confluence, the cells were washed twice with PBS by gently shaking the cell culture flask. This step was required to remove dead cells and debris. The cells were released with 0.05% trypsin-EDTA solution (Thermo Fisher Scientific, Waltham, MA), centrifuged (5 min, 500*g*) to remove the supernatant, and resuspended in 1× Dulbecco's phosphate buffered saline (DPBS, Thermo Fisher Scientific, Waltham, MA). To track the cell trajectories in the i^{2}FCS device, the cells were stained with either 3 μM CellTracker Green or 3 μM CellTracker Orange (Thermo Fisher Scientific, Waltham, MA) for 30 minutes at 37 °C and then washed and resuspended in culture medium. The cells were counted with a Countess 2 (Thermo Fisher Scientific, Waltham, MA) and diluted to 10^4 cells per mL in culture medium. After dilution, the exact number of cells was confirmed with a Nageotte counting chamber (Hausser Scientific, Horsham, PA). Variable numbers (10, 50, 100, and 200) of cancer cells were spiked into 0.015% (v/v) ferrofluid for spiking experiments.

Recovery rate and purity calculation of i^{2}FCS

Cells collected from the CTC outlet and WBC outlet were stained with 2 μM DAPI (Thermo Fisher Scientific, Waltham, MA) to stain the cell nucleus, and counted with a Nageotte counting chamber. Cells with a CellTracker (Green/Orange) signal were identified as cancer cells, while other cells only expressing a DAPI signal were identified as WBCs. The recovery rate of i^{2}FCS was calculated by $(N_{\text{cancer\_cell@CTC\_outlet}}/(N_{\text{cancer\_cell@CTC\_outlet}} + N_{\text{cancer\_cell@WBC\_outlet}})) \times 100\%$. The purity was characterized by the WBC carryover $N_{\text{WBC@CTC\_outlet}}$, the depletion rate $(1 - N_{\text{WBC@CTC\_outlet}}/N_{\text{Total\_WBC}}) \times 100\%$, and the log depletion rate $\log(N_{\text{Total\_WBC}}/N_{\text{WBC@CTC\_outlet}})$.

Cell morphology characterization

Cells suspended in PBS were deposited on a microscope slide and imaged with an inverted microscope (Axio Observer, Carl Zeiss, Germany) in bright field mode. Cell morphologies were analyzed with ImageJ software. The effective cell diameter was measured as the maximum Feret diameter of the cells under bright-field imaging.

Cell viability and proliferation characterization

The short-term cell viability of lung cancer cell line H1299 after i^{2}FCS processing was characterized with a live/dead assay (Thermo Fisher Scientific, Waltham, MA) following the manufacturer's protocol. All cells were alive at the start of the viability characterization. Dead cells and cell debris were removed by PBS washing after cell culture. For long-term proliferation, the isolated H1299 cells from the i^{2}FCS device were washed three times with cell culture medium to remove the ferrofluid, and then the cells were re-suspended in culture medium and transferred into a T25 flask (Corning, Corning, NY). The cells were then cultured at 37 °C (5% CO_2) under a humidified atmosphere. The cellular morphology was inspected every 24 hours.

Live subject statement

All experiments in this study were performed in compliance with the regulations of the United States Office for Human Research Protections and the University of Georgia Human Subjects Office. Human whole blood collected from healthy donors was purchased from a company (ZenBio, Durham, NC) for spiking experiments. Cancer patient blood was obtained from the University Cancer and Blood Center, LLC (Athens, GA) following a protocol approved by the Institutional Review Board (IRB) at the University of Georgia (VERSION00000869). Informed consent was obtained from the cancer patient participants.

Human sample processing

Complete blood count (CBC) reports of cancer patients' blood samples were used to determine the number of WBCs to optimize WBC labeling. Whole blood was firstly labeled with biotinylated antibodies including anti-CD45 (eBioscience, San Diego, CA), anti-CD45RA (eBioscience, San Diego, CA), anti-16 (eBioscience, San Diego, CA), anti-66b (Biolegend, San Diego, CA), and anti-CD3 (Biolegend, San Diego, CA) for 30 minutes at room temperature. The antibody-conjugated blood was lysed with RBC lysis buffer (eBioscience, San Diego, CA) for 5 minutes followed by centrifugation (500*g*, 5 minutes) at room temperature. After removing the supernatant, the cells were resuspended in 1× PBS and incubated with washed Dynabeads (Thermo Fisher Scientific, Waltham, MA) for 30 minutes on a rocker. All the labeling and washing procedures were performed following the manufacturer's protocol. The blood cells were suspended in the same volume of 0.015% (v/v) ferrofluid supplemented

with 0.1% (v/v) Pluronic F-68 surfactant (Thermo Fisher Scientific, Waltham, MA) before processing using the device.

CTC identification

After device processing, the isolated cells were concentrated through centrifugation (600*g*, 5 minutes) and immobilized onto poly-L-lysine (Sigma-Aldrich, St. Louis, Mo) coated glass slides. The isolated cells were fixed with 4% (w/v) paraformaldehyde (Santa Cruz Biotechnology, Dallas, TX) for 10 minutes and subsequently permeabilized with 0.1% (v/v) Triton X-100 (Alfa Aesar, Haverhill, MA) in PBS for 10 minutes at room temperature. The cells were then blocked with an Ultracruz blocking reagent (Santa Cruz Biotechnology, Dallas, TX) for 30 minutes at room temperature to block nonspecific binding sites. The cells were then immunostained overnight at 4 °C with primary antibodies including EpCAM–Alexa Fluor 488, N-cadherin–Alexa Fluor 594, vimentin–Alexa Fluor 647 (Santa Cruz Biotechnology, Dallas, TX), and CD45–PE (BD Bioscience, San Jose, CA). The cells were stored in mounting medium supplemented with DAPI (Fluoroshield™ with DAPI, Sigma-Aldrich, St. Louis, Mo).

Migration assay of isolated CTCs

The isolated CTCs were loaded into a microfluidic migration device for the single cell migration assay. 10% fetal bovine serum (FBS, Thermo Fisher Scientific, Waltham, MA), 20 ng mL^{-1} epidermal growth factor (EGF, Thermo Fisher Scientific, Waltham, MA), and 20 ng mL^{-1} basic fibroblast growth factor (bFGF, Thermo Fisher Scientific, Waltham, MA) were used as the chemoattractants for the CTCs, while 5 μg mL^{-1} Slit2 (Thermo Fisher Scientific, Waltham, MA) was used to inhibit the migration of WBCs. After cell loading, the migration assay was performed in an incubator (37 °C, 5% CO_2) for 24 hours. The cells were immunofluorescently stained in the device to identify their cell types.

Author contributions

L. M. conceived the study and supervised the research. Y. L. designed the i^2FCS and single cell migration device and its research. Y. L. performed the experiments. L. M. and Y. L. analyzed the data. W. Z. assisted in the device setup. R. C. assisted in the modeling and simulation. J. H., M. E., C. N. C. P, and P. G. N. assisted in the cancer patient recruitment and obtaining the samples. Y. L. and L. M. wrote the manuscript with input from all the authors.

Conflicts of interest

The i^2FCS and single cell migration device is the subject of the United States utility patent applications. Intellectual property related to the i^2FCS and single cell migration device is owned by the University of Georgia Research Foundation. Leidong Mao founded and owned FCS Technology LLC to commercialize the i^2FCS and single cell migration device. Leidong Mao and Wujun Zhao have financial interests in FCS Technology LLC, which is subject to certain restrictions under the university policy. The terms of this arrangement are being managed by the University of Georgia in accordance with its conflict of interest policies.

Acknowledgements

We are grateful to the donors of the blood samples for this study. This study is supported by the National Science Foundation under Grant Nos. 1150042, 1659525 and 1648035, the National Center for Advancing Translational Sciences of the National Institutes of Health under Award No. UL1TR002378, and the National Institute of Biomedical Imaging and Bioengineering of the National Institutes of Health under Award No. 1R41EB028191-01. The content is solely the responsibility of the authors and does not necessarily represent the official views of the National Institutes of Health.

References

1 M. Poudineh, E. H. Sargent, K. Pantel and S. O. Kelley, *Nat. Biomed. Eng.*, 2018, **2**, 72–84.
2 C. Alix-Panabieres and K. Pantel, *Nat. Biomed. Eng.*, 2017, **1**, 1–3.
3 J. Massague and A. C. Obenauf, *Nature*, 2016, **529**, 298–306.
4 M. G. Krebs, R. L. Metcalf, L. Carter, G. Brady, F. H. Blackhall and C. Dive, *Nat. Rev. Clin. Oncol.*, 2014, **11**, 129–144.
5 E. Heitzer, I. S. Haque, C. E. S. Roberts and M. R. Speicher, *Nat. Rev. Genet.*, 2019, **20**, 71–88.
6 N. Ma and S. S. Jeffrey, *Science*, 2020, **367**, 1424–1425.
7 S. Riethdorf, H. Fritsche, V. Muller, T. Rau, C. Schindibeck, B. Rack, W. Janni, C. Coith, K. Beck, F. Janicke, S. Jackson, T. Gornet, M. Cristofanilli and K. Pantel, *Clin. Cancer Res.*, 2007, **13**, 920–928.
8 A. Romiti, S. Raffa, R. Di Rocco, M. Roberto, A. Milano, A. Zullo, L. Leone, D. Ranieri, F. Mazzetta, E. Medda, I. Sarcina, V. Barucca, C. D'Antonio, V. Durante, M. Ferri, M. R. Torrisi and P. Marchetti, *J. Gastrointest. Liver Dis*, 2014, **23**, 279–284.
9 F. C. Bidard, D. J. Peeters, T. Fehm, F. Nole, R. Gisbert-Criado, D. Mavroudis, S. Grisanti, D. Generali, J. A. Garcia-Saenz, J. Stebbing, C. Caldas, P. Gazzaniga, L. Manso, R. Zamarchi, A. F. de Lascoiti, L. De Mattos-Arruda, M. Ignatiadis, R. Lebofsky, S. J. van Laere, F. Meier-Stiegen, M. T. Sandri, J. Vidal-Martinez, E. Politaki, F. Consoli, A. Bottini, E. Diaz-Rubio, J. Krell, S. J. Dawson, C. Raimondi, A. Rutten, W. Janni, E. Munzone, V. Caranana, S. A. Agelaki, C. Almici, L. Dirix, E. F. Solomayer, L. Zorzino, H. Johannes, J. S. Reis, K. Pantel, J. Y. Pierga and S. Michiels, *Lancet Oncol.*, 2014, **15**, 406–414.
10 A. W. Lambert, D. R. Pattabiraman and R. A. Weinberg, *Cell*, 2017, **168**, 670–691.
11 C. L. Chaffer and R. A. Weinberg, *Science*, 2011, **331**, 1559–1564.
12 M. Poudineh, P. Aldridge, S. Ahmed, B. J. Green, L. Kermanshah, V. Nguyen, C. Tu, R. M. Mohamadi, R. K. Nam,

A. Hansen, S. S. Sridhar, A. Finelli, N. E. Fleshner, A. M. Joshua, E. H. Sargent and S. O. Kelley, *Nat. Nanotechnol.*, 2017, **12**, 274–281.
13 Y. H. Cheng, Y. C. Chen, E. Lin, R. Brien, S. Jung, Y. T. Chen, W. Lee, Z. Hao, S. Sahoo, H. Min Kang, J. Cong, M. Burness, S. Nagrath and M. Wicha, *Nat. Commun.*, 2019, **10**, 2163.
14 E. Sahai, *Nat. Rev. Cancer*, 2007, **7**, 737–749.
15 L. Keller and K. Pantel, *Nat. Rev. Cancer*, 2019, **19**, 553–567.
16 B. Strilic and S. Offermanns, *Cancer Cell*, 2017, **32**, 282–293.
17 P. S. Steeg, *Nat. Rev. Cancer*, 2016, **16**, 201–218.
18 P. Friedl and K. Wolf, *Nat. Rev. Cancer*, 2003, **3**, 362–374.
19 C. D. Paul, P. Mistriotis and K. Konstantopoulos, *Nat. Rev. Cancer*, 2017, **17**, 131–140.
20 C. Alix-Panabieres and K. Pantel, *Nat. Rev. Cancer*, 2014, **14**, 623–631.
21 M. Poudineh, E. H. Sargent, K. Pantel and S. O. Kelley, *Nat. Biomed. Eng.*, 2018, **2**, 72–84.
22 C. Alix-Panabieres, K. Bartkowiak and K. Pantel, *Mol. Oncol.*, 2016, **10**, 443–449.
23 Y. Zhang, W. Zhang and L. Qin, *Angew. Chem., Int. Ed.*, 2014, **53**, 2344–2348.
24 C. L. Yankaskas, K. N. Thompson, C. D. Paul, M. I. Vitolo, P. Mistriotis, A. Mahendra, V. K. Bajpai, D. J. Shea, K. M. Manto, A. C. Chai, N. Varadarajan, A. Kontrogianni-Konstantopoulos, S. S. Martin and K. Konstantopoulos, *Nat. Biomed. Eng.*, 2019, **3**, 452–465.
25 Y. C. Chen, S. G. Allen, P. N. Ingram, R. Buckanovich, S. D. Merajver and E. Yoon, *Sci. Rep.*, 2015, **5**, 9980.
26 I. Y. Wong, S. Javaid, E. A. Wong, S. Perk, D. A. Haber, M. Toner and D. Irimia, *Nat. Mater.*, 2014, **13**, 1063–1071.
27 M. Poudineh, M. Labib, S. Ahmed, L. N. Nguyen, L. Kermanshah, R. M. Mohamadi, E. H. Sargent and S. O. Kelley, *Angew. Chem., Int. Ed.*, 2017, **56**, 163–168.
28 D. Di Carlo, D. Irimia, R. G. Tompkins and M. Toner, *Proc. Natl. Acad. Sci. U. S. A.*, 2007, **104**, 18892–18897.
29 H. Amini, W. Lee and D. Di Carlo, *Lab Chip*, 2014, **14**, 2739–2761.
30 D. Di Carlo, *Lab Chip*, 2009, **9**, 3038–3046.
31 R. E. Rosensweig, *Ferrohydrodynamics*, Cambridge University Press, Cambridge, 1985.
32 W. Zhao, Y. Liu, B. D. Jenkins, R. Cheng, B. N. Harris, W. Zhang, J. Xie, J. R. Murrow, J. Hodgson, M. Egan, A. Bankey, P. G. Nikolinakos, H. Y. Ali, K. Meichner, L. A. Newman, M. B. Davis and L. Mao, *Lab Chip*, 2019, **19**, 1860–1876.
33 Y. Liu, W. Zhao, R. Cheng, B. N. Harris, J. R. Murrow, J. Hodgson, M. Egan, A. Bankey, P. G. Nikolinakos, T. Laver, K. Meichner and L. Mao, *Lab Chip*, 2021, **21**, 1706–1723.
34 A. Mishra, T. D. Dubash, J. F. Edd, M. K. Jewett, S. G. Garre, N. M. Karabacak, D. C. Rabe, B. R. Mutlu, J. R. Walsh and R. Kapur, *Proceedings of the National Academy of Sciences*, 2020, **117**, 16839–16847.
35 E. Ozkumur, A. M. Shah, J. C. Ciciliano, B. L. Emmink, D. T. Miyamoto, E. Brachtel, M. Yu, P. I. Chen, B. Morgan, J. Trautwein, A. Kimura, S. Sengupta, S. L. Stott, N. M. Karabacak, T. A. Barber, J. R. Walsh, K. Smith, P. S. Spuhler, J. P. Sullivan, R. J. Lee, D. T. Ting, X. Luo, A. T. Shaw, A. Bardia, L. V. Sequist, D. N. Louis, S. Maheswaran, R. Kapur, D. A. Haber and M. Toner, *Sci. Transl. Med.*, 2013, **5**, 179ra147.
36 F. Fachin, P. Spuhler, J. M. Martel-Foley, J. F. Edd, T. A. Barber, J. Walsh, M. Karabacak, V. Pai, M. Yu, K. Smith, H. Hwang, J. Yang, S. Shah, R. Yarmush, L. V. Sequist, S. L. Stott, S. Maheswaran, D. A. Haber, R. Kapur and M. Toner, *Sci. Rep.*, 2017, **7**, 10936.
37 M. A. Nieto, R. Y. Huang, R. A. Jackson and J. P. Thiery, *Cell*, 2016, **166**, 21–45.
38 J. P. Thiery, H. Acloque, R. Y. Huang and M. A. Nieto, *Cell*, 2009, **139**, 871–890.
39 J. P. Thiery, *Nat. Rev. Cancer*, 2002, **2**, 442–454.
40 Y. Liu, W. Zhao, R. Cheng, A. Puig, J. Hodgson, M. Egan, C. N. Cooper Pope, P. G. Nikolinakos and L. Mao, *Lab Chip*, 2021, **21**, 2738–2750.
41 J. J. Nieva and P. Kuhn, *Future Oncol.*, 2012, **8**, 989–998.
42 D. J. Peeters, G. G. Van den Eynden, P. J. van Dam, A. Prove, I. H. Benoy, P. A. van Dam, P. B. Vermeulen, P. Pauwels, M. Peeters, S. J. Van Laere and L. Y. Dirix, *Br. J. Cancer*, 2011, **104**, 1472–1477.
43 R. A. Harouaka, M. Nisic and S. Y. Zheng, *J. Lab. Autom.*, 2013, **18**, 455–468.
44 D. Marrinucci, K. Bethel, D. Lazar, J. Fisher, E. Huynh, P. Clark, R. Bruce, J. Nieva and P. Kuhn, *J. Oncol.*, 2010, **2010**, 861341.
45 M. Yu, A. Bardia, B. Wittner, S. L. Stott, M. E. Smas, D. T. Ting, S. J. Isakoff, J. C. Ciciliano, M. N. Wells, A. M. Shah, K. F. Concannon, M. C. Donaldson, L. V. Sequist, E. Brachtel, D. Sgroi, J. Baselga, S. Ramaswamy, M. Toner, D. A. Haber and S. Maheswaran, *Science*, 2013, **339**, 580–584.
46 S. L. Stott, C.-H. Hsu, D. I. Tsukrov, M. Yu, D. T. Miyamoto, B. A. Waltman, S. M. Rothenberg, A. M. Shah, M. E. Smas, G. K. Korir, F. P. Floyd, A. J. Gilman, J. B. Lord, D. Winokur, S. Springer, D. Irimia, S. Nagrath, L. V. Sequist, R. J. Lee, K. J. Isselbacher, S. Maheswaran, D. A. Haber and M. Toner, *Proc. Natl. Acad. Sci. U. S. A.*, 2010, **107**, 18392–18397.
47 R. J. Petrie, A. D. Doyle and K. M. Yamada, *Nat. Rev. Mol. Cell Biol.*, 2009, **10**, 538–549.
48 E. T. Roussos, M. Balsamo, S. K. Alford, J. B. Wyckoff, B. Gligorijevic, Y. Wang, M. Pozzuto, R. Stobezki, S. Goswami, J. E. Segall, D. A. Lauffenburger, A. R. Bresnick, F. B. Gertler and J. S. Condeelis, *J. Cell Sci.*, 2011, **124**, 2120–2131.
49 E. T. Roussos, J. S. Condeelis and A. Patsialou, *Nat. Rev. Cancer*, 2011, **11**, 573–587.
50 J. Y. Wu, L. Feng, H. T. Park, N. Havlioglu, L. Wen, H. Tang, K. B. Bacon, Z. Jiang, X. Zhang and Y. Rao, *Nature*, 2001, **410**, 948–952.
51 L. Boneschansker, J. Yan, E. Wong, D. M. Briscoe and D. Irimia, *Nat. Commun.*, 2014, **5**, 4787.
52 K. Wolf, S. Alexander, V. Schacht, L. M. Coussens, U. H. von Andrian, J. van Rheenen, E. Deryugina and P. Friedl, *Semin. Cell Dev. Biol.*, 2009, **20**, 931–941.
53 B. Weigelin, G. J. Bakker and P. Friedl, *Intravital*, 2012, **1**, 32–43.

54 P. C. Benias, R. G. Wells, B. Sackey-Aboagye, H. Klavan, J. Reidy, D. Buonocore, M. Miranda, S. Kornacki, M. Wayne, D. L. Carr-Locke and N. D. Theise, *Sci. Rep.*, 2018, **8**, 4947.
55 E. Sahai, *Curr. Opin. Genet. Dev.*, 2005, **15**, 87–96.
56 K. Wolf, I. Mazo, H. Leung, K. Engelke, U. H. von Andrian, E. I. Deryugina, A. Y. Strongin, E. B. Brocker and P. Friedl, *J. Cell Biol*, 2003, **160**, 267–277.
57 E. Sahai and C. J. Marshall, *Nat. Cell Biol.*, 2003, **5**, 711–719.
58 W. J. Zhao, R. Cheng, S. H. Lim, J. R. Miller, W. Z. Zhang, W. Tang, J. Xie and L. D. Mao, *Lab Chip*, 2017, **17**, 2243–2255.
59 Y. Liu, W. Zhao, R. Cheng, M. Logun, M. D. M. Zayas-Viera, L. Karumbaiah and L. Mao, *Lab Chip*, 2020, **20**, 3187–3201.